Second harmonic imaging of antiferromagnetic domains and confirmation of absence of ferroaxial twins in $MnTiO_3$

Daiki Sekine,[1] Tatsuki Sato,[2] Yusuke Tokunaga,[2] Taka-hisa Arima,[2] and Masakazu Matsubara[1,3,4,*]

[1]*Department of Physics, Tohoku University, Sendai 980-8578, Japan*

[2]*Department of Advanced Materials Science, University of Tokyo, Kashiwa 277-8561, Japan*

[3]*Center for Science and Innovation in Spintronics, Tohoku University, Sendai 980-8577, Japan*

[4]*PRESTO, Japan Science and Technology Agency (JST), Kawaguchi 332-0012, Japan*

(Received 21 November 2023; accepted 28 May 2024; published 14 June 2024)

Multipoles in a material, which describe the degrees of freedom of electrons, have recently attracted much attention from the perspective of a unified understanding of diverse physical phenomena. Therefore, demand has been increasing for probes that can detect various types of multipoles. Here, we report the detection of multiple multipoles in collinear antiferromagnet $MnTiO_3$ using optical second harmonic generation (SHG). Utilizing SHG selection rules and an imaging technique, we detect ferroaxial and antiferromagnetic orders and visualize their domains, and show that SHG is a powerful tool for the simultaneous observation of underlying multipoles with different symmetries.

DOI: 10.1103/PhysRevMaterials.8.064406

I. INTRODUCTION

Exploring the relationship between the symmetries of a material and their functionalities is a central topic in modern condensed matter physics. Recent studies have shown that multipoles, which describe the spatial distributions of electric charge and magnetic moment, are useful quantities for describing, understanding, and predicting diverse physical phenomena [1,2]. In particular, the multipoles that break both space-inversion ($\mathscr{P}$) and time-reversal ($\mathscr{T}$) symmetries—i.e., the magnetic monopole (MM), the magnetic quadrupole (MQ), and the magnetic toroidal dipole (MTD)—have attracted attention because they induce magnetoelectric (ME) cross-coupling phenomena such as linear ME effects [3–5] and nonreciprocal optical effects [6–8]. A contrasting multipole is the electric toroidal dipole (ETD), which breaks neither $\mathscr{P}$ nor $\mathscr{T}$ [9]; this multipole is related to the ferroaxial (or ferrorotational) order that is characterized by a rotational electric dipole arrangement (or rotational crystal distortion) [9–11]. In many cases, multipoles with different symmetries are detected using different experimental techniques [7,8,10–17], but this makes it difficult to explore the relationships among multipoles with different symmetries. Therefore, there is strong demand for developing probes that can directly detect a wide variety of multipoles and reveal their mutual couplings.

In this paper, we focus on the detection of multipoles in the ilmenite $MnTiO_3$ using optical second harmonic generation (SHG). $MnTiO_3$ is an antiferromagnet that possesses multiple multipoles, i.e., MM, MQ, and MTD in the antiferromagnetic (AFM) phase as well as ETD in the whole temperature range. Using SHG selection rules and an imaging technique, we spatially resolve multipolar domain structures and clarify their characteristics.

*Contact author: m-matsubara@tohoku.ac.jp

II. MULTIPOLES IN $MnTiO_3$

$MnTiO_3$ crystallizes with trigonal symmetry with the centrosymmetric point group $\bar{3}$ at room temperature [Fig. 1(a)] [18]. Buckled honeycomb layers consisting of magnetic Mn^{2+} ions ($S = 5/2$) and those of nonmagnetic Ti^{4+} ions are stacked alternately along the threefold c axis. The rotational displacements of O^{2-} ions around Mn^{2+} and Ti^{4+} ions from the {110} planes [dotted lines in Fig. 1(a)] break the c-glide plane parallel to {110}, which leads to the presence of ETD related to the ferroaxial order [11]. Below the Néel temperature $T_N = 65$ K, the spin moments on Mn^{2+} ions are arranged along the c axis to form collinear AFM order, which is characterized by the Néel vector $\boldsymbol{L}$ [Fig. 1(b)]. The AFM spin structure retains the threefold symmetry but breaks both $\mathscr{P}$ and $\mathscr{T}$, which leads to a symmetry reduction to the magnetic point group $\bar{3}'$ [19,20]. The antiparallel spin is represented by a superposition of MM and MQ with possible combinations of (MM, MQ) = (+, +), (−, −) [21]. Furthermore, adjacent MnO_6 clusters with opposite spin moments have opposite chirality, which induces MTD along the c axis [7]. Because the sign of MTD is determined by those of ETD and $\boldsymbol{L}$ [7], four types of multipolar domains may exist below T_N, i.e., (ETD, MM, MQ, MTD) = (+, +, +, +), (+, −, −, −), (−, +, +, −), (−, −, −, +). This situation differs from the case of Cr_2O_3, which has a similar collinear AFM spin structure to that of $MnTiO_3$. In Cr_2O_3, both ETD and MTD exhibit staggered order because of the presence of twofold axes perpendicular to the c axis [7], resulting in the absence of macroscopic ETD and MTD.

III. OPTICAL SECOND HARMONIC GENERATION

To detect these multipoles with different symmetries in $MnTiO_3$, we use SHG selection rules beyond the electric-dipole (ED) approximation. In the ED approximation, SHG

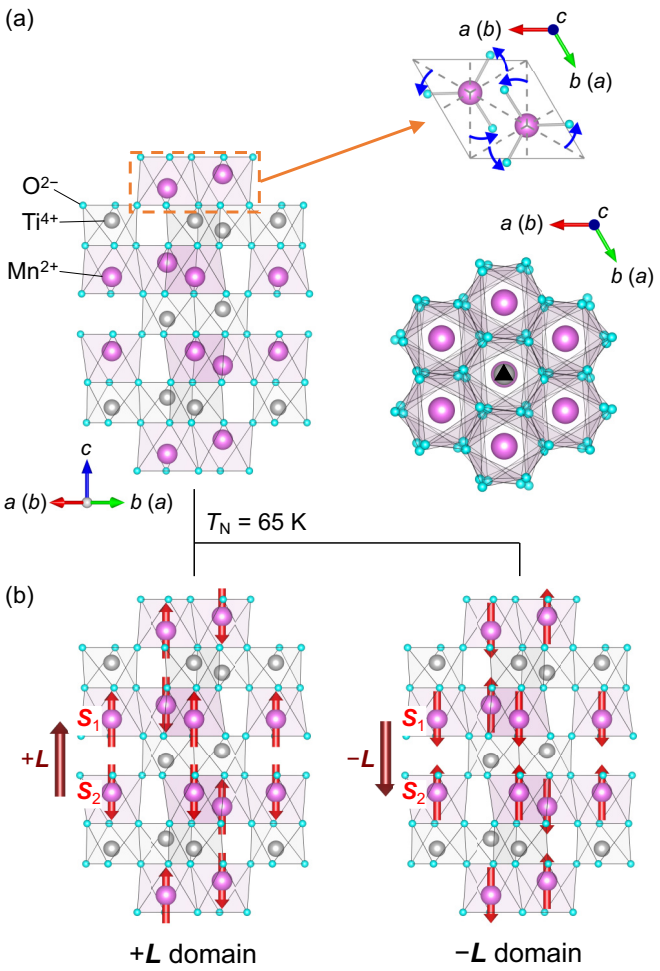

FIG. 1. Crystallographic and magnetic structures of $MnTiO_3$ projected along [110] and [001] (a) above T_N and (b) below T_N. In both the paramagnetic and AFM phases, the rotational displacements of O^{2-} ions around Mn^{2+} and Ti^{4+} ions from the {110} planes (dotted lines) break mirror symmetry parallel to those planes, which leads to the presence of the ETD related to the ferroaxial order. In the AFM phase, the antiparallel spin pair ($\boldsymbol{S}_1$ and $\boldsymbol{S}_2$) of two Mn^{2+} ions is described by the Néel vector $\boldsymbol{L} \equiv \boldsymbol{S}_1 - \boldsymbol{S}_2$ and can be decomposed into MM and MQ. In addition, a spin in the chiral MnO_6 cluster breaks both $\mathscr{P}$ and $\mathscr{T}$, which can be regarded as MTD. The equilateral triangle marked on the central Ti^{4+} ion indicates the threefold axis.

is allowed only in noncentrosymmetric systems such as ferroelectrics, surfaces, and interfaces [22]. This so-called ED-SHG can be expressed as

$$\boldsymbol{P}^{\mathrm{ED}}(2\omega) \propto \left(\chi^{(i)eee} + \chi^{(c)eee}\right) : \boldsymbol{E}(\omega)\boldsymbol{E}(\omega), \tag{1}$$

where $\boldsymbol{P}^{\mathrm{ED}}(2\omega)$ is the nonlinear polarization oscillating at 2ω, $\boldsymbol{E}(\omega)$ is the electric field of incident light oscillating at ω, and $\chi^{(i)eee}$ and $\chi^{(c)eee}$ are the time-invariant (i-type) and time-noninvariant (c-type) nonlinear susceptibilities related to the crystallographic and magnetic contributions to ED-SHG, respectively [23,24]. In contrast, SHG processes including higher-order multipole contributions such as magnetic-dipole (MD) and electric-quadrupole (EQ) transitions are allowed even in centrosymmetric media [23–30]. Because the MD- and EQ-SHGs show the same polarization dependence [31], we only consider the MD-SHG in the following discussion. The MD-SHG $\boldsymbol{P}^{\mathrm{MD}}(2\omega)$ is induced by the electric field $\boldsymbol{E}(\omega)$ and magnetic field $\boldsymbol{H}(\omega)$ of incident light and can be expressed as follows [23,24],

$$\boldsymbol{P}^{\mathrm{MD}}(2\omega) \propto \left(\chi^{(i)eem} + \chi^{(c)eem}\right) : \boldsymbol{E}(\omega)\boldsymbol{H}(\omega), \tag{2}$$

where $\chi^{(i)eem}$ and $\chi^{(c)eem}$ are the nonlinear susceptibilities related to the crystallographic and magnetic contributions to MD-SHG. The contribution from another MD-SHG process expressed as $\boldsymbol{M}(2\omega) \propto \chi^{mee} : \boldsymbol{E}(\omega)\boldsymbol{E}(\omega)$ is negligible because our SHG wavelength of 400 nm is related to the charge transfer transition between O $2p$ and Mn $3d$ where the MD transition is forbidden. Above T_N, $MnTiO_3$ has a centrosymmetric crystal structure but the i-type MD-SHG is allowed. Below T_N, the collinear AFM order breaking both $\mathscr{P}$ and $\mathscr{T}$ allows the c-type ED-SHG in addition to the i-type MD-SHG. The c-type MD-SHG is forbidden by the symmetry because of the conservation of the AFM structure under the combined inversion-time reversal operation $\bar{1}'$ [32]. The nonzero MD-SHG and ED-SHG tensor components above and below T_N are summarized in Table I.

In materials with a threefold symmetry, circularly polarized fundamental light propagating along the threefold axis is converted only to countercircularly polarized SHG because of angular momentum conservation [33]. In the present case, when right-handed circularly polarized (RCP) fundamental light is incident along the c axis of $MnTiO_3$, left-handed circularly polarized (LCP) SHG light is emitted, whose intensity above T_N can be written as

$$I^{T>T_N}_{\mathrm{RCP}(\omega)\text{-}\mathrm{LCP}(2\omega)} \propto \left|\chi^{(i)}_{m1}\right|^2 + \left|\chi^{(i)}_{m2}\right|^2 + 2\,\mathrm{Im}\left(\chi^{(i)}_{m1}\chi^{(i)*}_{m2}\right). \tag{3}$$

As discussed in detail in the Supplemental Material [31], the term $\mathrm{Im}(\chi^{(i)}_{m1}\chi^{(i)*}_{m2})$ gives opposite signs for opposite ETDs, thus distinguishing opposite ferroaxial domains as a difference in SHG intensity [31].

Below T_N, the SHG intensity in the aforementioned configuration is expressed as

$$\begin{aligned} I^{T<T_N}_{\mathrm{RCP}(\omega)\text{-}\mathrm{LCP}(2\omega)} \propto{}& \left|\chi^{(i)}_{m1}\right|^2 + \left|\chi^{(i)}_{m2}\right|^2 + \left|\chi^{(c)}_{e1}\right|^2 + \left|\chi^{(c)}_{e2}\right|^2 \\ &+ 2\,\mathrm{Im}\left(\chi^{(i)}_{m1}\chi^{(i)*}_{m2} + \chi^{(c)}_{e1}\chi^{(c)*}_{e2}\right) \\ &+ 2\,\mathrm{Im}\left(\chi^{(i)}_{m1}\chi^{(c)*}_{e1} + \chi^{(i)}_{m2}\chi^{(c)*}_{e2}\right) \\ &- 2\,\mathrm{Re}\left(\chi^{(i)}_{m1}\chi^{(c)*}_{e2} - \chi^{(i)}_{m2}\chi^{(c)*}_{e1}\right). \end{aligned} \tag{4}$$

The last two terms, which represent the interference between the nonmagnetic tensor $\chi^{(i)}$ and the magnetic tensor $\chi^{(c)}$, play a significant role in distinguishing the AFM 180° (i.e., $\boldsymbol{L}$) domains [25] because only $\chi^{(c)}$ changes sign for the opposite $\boldsymbol{L}$. Consequently, the SHG signal gives a difference in intensity of

$$\begin{aligned} \Delta I^{T<T_N}_{\mathrm{RCP}(\omega)\text{-}\mathrm{LCP}(2\omega)} \propto 4\big[&\mathrm{Im}\left(\chi^{(i)}_{m1}\chi^{(c)*}_{e1} + \chi^{(i)}_{m2}\chi^{(c)*}_{e2}\right) \\ &-\mathrm{Re}\left(\chi^{(i)}_{m1}\chi^{(c)*}_{e2} - \chi^{(i)}_{m2}\chi^{(c)*}_{e1}\right)\big] \end{aligned} \tag{5}$$

between the AFM 180° domains below T_N [Fig. 2(a)]. Since $\chi^{(c)}_{e1}$ and $\chi^{(c)}_{e2}$ are proportional to the magnetic order parameter ($\boldsymbol{L}$), it is possible to investigate the AFM properties by measuring the temperature dependence and spatial distribution of the SHG signal.

TABLE I. Nonzero time-invariant (i-type) and time-noninvariant (c-type) SHG tensor components in $MnTiO_3$ allowed above and below T_N. These are derived from the point group $\bar{3}$ and magnetic point group $\bar{3}'$ [32]. Only the tensor components for light incident along the c axis are listed.

	$T < T_N$	$T > T_N$
(Magnetic) point group	$\bar{3}'$	$\bar{3}$
$\chi_{ijk}^{(i)eem}$	$\chi_{m1}^{(i)} \equiv \chi_{xxx}^{(i)eem} = -\chi_{xyy}^{(i)eem} = -\chi_{yxy}^{(i)eem} = -\chi_{yyx}^{(i)eem}$ $\chi_{m2}^{(i)} \equiv \chi_{yyy}^{(i)eem} = -\chi_{xxy}^{(i)eem} = -\chi_{xyx}^{(i)eem} = -\chi_{yxx}^{(i)eem}$	$\chi_{m1}^{(i)} \equiv \chi_{xxx}^{(i)eem} = -\chi_{xyy}^{(i)eem} = -\chi_{yxy}^{(i)eem} = -\chi_{yyx}^{(i)eem}$ $\chi_{m2}^{(i)} \equiv \chi_{yyy}^{(i)eem} = -\chi_{xxy}^{(i)eem} = -\chi_{xyx}^{(i)eem} = -\chi_{yxx}^{(i)eem}$
$\chi_{ijk}^{(c)eee}$	$\chi_{e1}^{(c)} \equiv \chi_{xxx}^{(c)eee} = -\chi_{xyy}^{(c)eee} = -\chi_{yxy}^{(c)eee} = -\chi_{yyx}^{(c)eee}$ $\chi_{e2}^{(c)} \equiv \chi_{yyy}^{(c)eee} = -\chi_{xxy}^{(c)eee} = -\chi_{xyx}^{(c)eee} = -\chi_{yxx}^{(c)eee}$	

IV. EXPERIMENTAL RESULTS AND DISCUSSIONS

A. Experimental setup

A single crystal of $MnTiO_3$ was grown by a floating zone method in Ar flow [7]. The crystal was then cut and polished into a 230-μm-thick plate with large (001) surfaces of 4.9 mm × 4.3 mm, which was mounted on a copper plate with a hole in a cryostat [Fig. 2(b)]. SHG measurements were performed with light pulses from a Ti:sapphire laser with a central wavelength of 800 nm, a pulse width of 130 fs, and a repetition rate of 1 kHz. The plate was irradiated at the normal incidence, and the transmitted SHG image was recorded with a charge-coupled device (CCD) camera [Fig. 2(a)]. The laser power and the focal diameter were ∼40 mW and ∼2.5 mm, respectively, unless stated otherwise. A polarizer, a half-wave plate, and a quarter-wave plate before the sample were used to generate the circularly polarized incident light, and a quarter-wave plate and an analyzer after the sample were used to extract the circularly polarized SHG component. We confirmed the quadratic dependence of the SHG intensity on the power of the fundamental light both above and below T_N [Fig. 2(c)].

B. SHG images of $MnTiO_3$

The SHG image at 80 K ($T > T_N$) shows a nearly homogeneous spatial distribution, except for some bright lines due to cracks and scratches on the surfaces discernible also in the conventional optical microscope image [Fig. 3(a)]. This indicates the absence of ferroaxial twins [31], which agrees with a recent nonreciprocal optical experiment [34]. In contrast, the SHG image at 45 K ($T < T_N$) after zero-field cooling clearly shows a spatial inhomogeneity [Fig. 3(b)]. This multidomain structure originates from the interference between $\chi_m^{(i)}$ and $\chi_e^{(c)}$, as discussed above, and indicates the existence of AFM 180° domains composed of MM, MQ, and MTD. Considering the ferroaxial single domain, the AFM 180° domains are regarded as two types of magnetic (toroidal) multipolar domains, i.e., (MM, MQ, MTD) = (+, +, +), (−, −, −).

The SHG image below T_N changed every time when the temperature was increased and decreased across T_N, indicating no memory effect across T_N [31]. The AFM domain structure is similar to those of other antiferromagnets such as $YMnO_3$ [35]. The typical lateral dimension of the AFM domains in $MnTiO_3$ is submillimeter, which is smaller than that in Cr_2O_3 (∼1 mm) [25]. In general, materials with larger exchange energy are preferable for forming larger domains to reduce the energy cost at domain walls. The values of the in-plane nearest-neighbor exchange energy in $MnTiO_3$ and Cr_2O_3 are reported to be −0.627 and −3.27 meV [36,37], respectively, which may explain the smaller in-plane AFM domain in $MnTiO_3$.

C. Temperature dependence of SHG intensity

The AFM origin of the multidomain structures can be clearly seen by tracking the temperature dependence of the

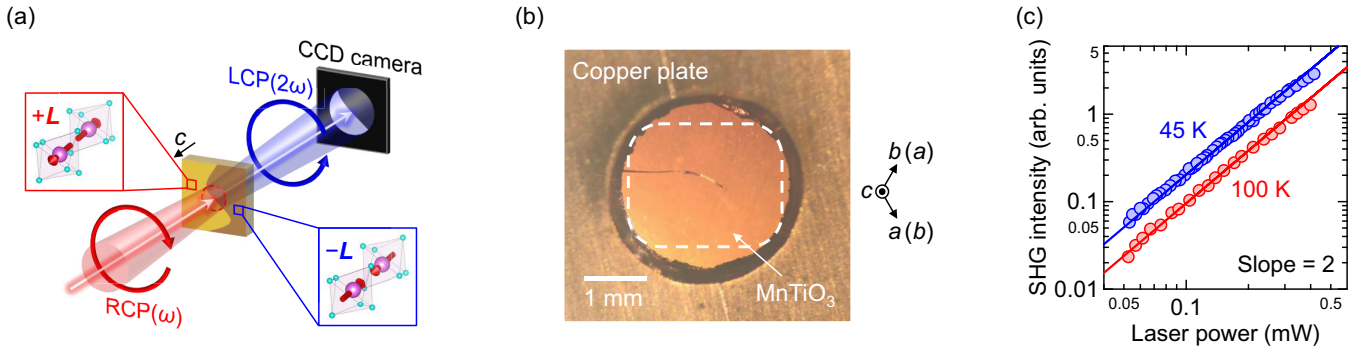

FIG. 2. (a) Schematic of experimental setup. RCP-fundamental light [RCP(ω)] propagating along the c axis of $MnTiO_3$ generates LCP-SHG [LCP(2ω)]. AFM 180° domains ($+\boldsymbol{L}$ and $-\boldsymbol{L}$ domains) give a contrast in SHG intensity. (b) Optical microscope image of $MnTiO_3$. SHG images were taken in the region surrounded by the dashed line. (c) Log-log plots of SHG intensity as a function of incident laser power at 100 and 45 K.

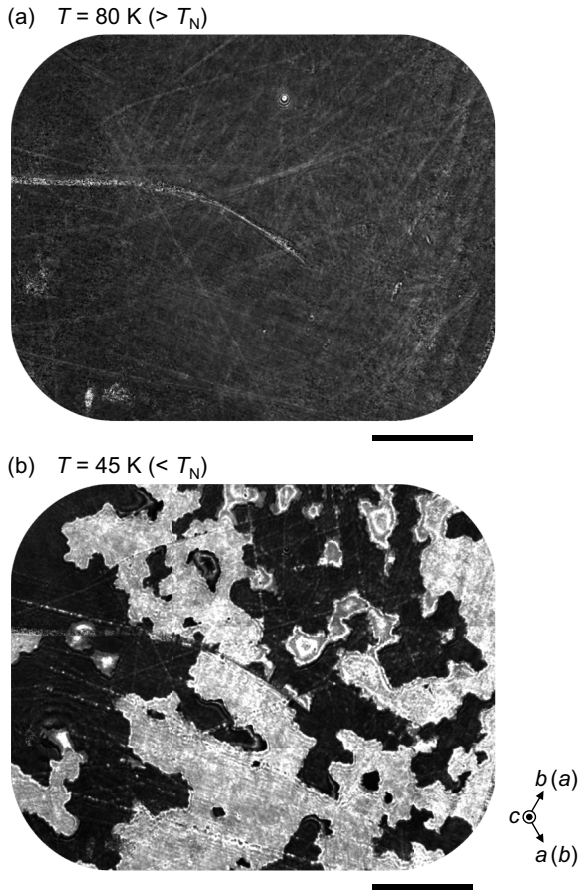

FIG. 3. SHG images taken in RCP(ω)-LCP(2ω) configuration at (a) 80 K (above T_N) and (b) 45 K (below T_N). The homogeneous image in (a) indicates a ferroaxial single domain, whereas the bright and dark regions in (b) correspond to AFM $+\boldsymbol{L}$ and $-\boldsymbol{L}$ domains, respectively. Scale bar: 500 μm.

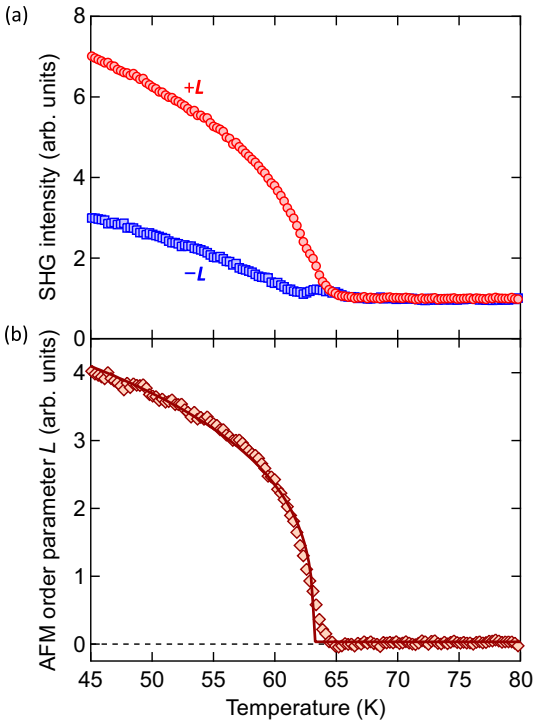

FIG. 4. Temperature dependence of (a) SHG intensity for $+\boldsymbol{L}$ (circles) and $-\boldsymbol{L}$ (squares) domains in Fig. 3(b), and (b) the AFM order parameter L calculated from (a) using Eq. (5). L is fitted with the power law $L \propto (1 - T/T_N)^{\beta}$ with $\beta = 0.32$ and $T_N = 63.2$ K. The SHG data were taken in a warming run.

spatial average intensity of bright (circles) and dark (squares) areas of the SHG image [Fig. 4(a)]. Above T_N the SHG intensities are temperature independent and almost the same for both areas but they clearly show a difference below T_N, reflecting the development of the AFM order of the opposite $\boldsymbol{L}$. According to Eq. (5), this can be estimated directly by taking the difference in the two SHG intensities, assuming that the temperature dependence of $\chi^{(i)}_{m1}$ and $\chi^{(i)}_{m2}$ is negligibly small. Figure 4(b) shows the temperature dependence of the AFM order parameter L. This can be approximately fitted to a power law $L \propto (1 - T/T_N)^{\beta}$ with the exponent $\beta = 0.32$, which is consistent with the value of the sublattice magnetization obtained by neutron scattering measurements [38]. Compared to the bulk value of $T_N = 65$ K, the slightly lower one of $T_N = 63.2$ K obtained from the fitting may be ascribed to a deviation between the actual temperature of the sample and the temperature monitor, or it may reflect T_N near the sample surface, because the present SHG only detects signals from tens of nanometers on the backside of the sample because of the strong absorption at the SHG wavelength (400 nm) [7]. This could be another tool for investigating the depth-dependent nature of AFM orders and their domains by tuning the SHG wavelength.

V. CONCLUSIONS

In summary, we detected multiple multipoles and visualized their domain structures in $MnTiO_3$ by using the SHG selection rules beyond the ED approximation. We revealed the absence of ferroaxial twins related to the ETD order above T_N and multi-AFM domains related to the MM, MQ, and MTD orders below T_N, whose order parameter is consistent with the behavior of the sublattice magnetization. Our study shows that SHG can detect multipoles with different symmetries (odd/even parities and electric/magnetic multipoles). This feature is critically important for visualizing various multipole domains and their mutual couplings, and also for searching new functionalities at domain walls [39].

The data are available from the authors upon reasonable request.

ACKNOWLEDGMENTS

This work was supported by JSPS KAKENHI (Grants No. 24H01639, No. 23H04868, No. 24H00413, No. 21H04649, No. 22K18962, No. 19H01835, and No. JP19H05826), JST PRESTO (Grant No. JPMJPR23H9), the Asahi Glass Foundation, the Research Foundation for Opto-Science and Technology, the Murata Science Foundation, the Mayekawa Houonkai Foundation, the TEPCO Memorial Foundation,

and TIA-Kakehashi (Grant No. TK23-019). D.S. acknowledges support from GP-Spin at Tohoku University, JST, the establishment of university fellowships towards the creation of science technology innovation (Grant No. JPMJFS2102), JST SPRING (Grant No. JPMJSP2114), and Grant-in-Aid for JSPS Fellows (Grant No. 23KJ0141).

[1] S. Hayami, M. Yatsushiro, Y. Yanagi, and H. Kusunose, Phys. Rev. B **98**, 165110 (2018).
[2] H. Watanabe and Y. Yanase, Phys. Rev. B **98**, 245129 (2018).
[3] D. N. Astrov, J. Exptl. Theoret. Phys. (U.S.S.R.) **38**, 984 (1960) [Sov. Phys. JETP **11**, 708 (1960)].
[4] V. J. Folen, G. T. Rado, and E. W. Stalder, Phys. Rev. Lett. **6**, 607 (1961).
[5] N. Mufti, G. R. Blake, M. Mostovoy, S. Riyadi, A. A. Nugroho, and T. T. M. Palstra, Phys. Rev. B **83**, 104416 (2011).
[6] J. H. Jung, M. Matsubara, T. Arima, J. P. He, Y. Kaneko, and Y. Tokura, Phys. Rev. Lett. **93**, 037403 (2004).
[7] T. Sato, N. Abe, S. Kimura, Y. Tokunaga, and T. Arima, Phys. Rev. Lett. **124**, 217402 (2020).
[8] K. Kimura, T. Katsuyoshi, Y. Sawada, S. Kimura, and T. Kimura, Commun. Mater. **1**, 39 (2020).
[9] S. Hayami, R. Oiwa, and H. Kusunose, J. Phys. Soc. Jpn. **91**, 113702 (2022).
[10] W. Jin, E. Drueke, S. Li, A. Admasu, R. Owen, M. Day, K. Sun, S.-W. Cheong, and L. Zhao, Nat. Phys. **16**, 42 (2020).
[11] T. Hayashida, Y. Uemura, K. Kimura, S. Matsuoka, D. Morikawa, S. Hirose, K. Tsuda, T. Hasegawa, and T. Kimura, Nat. Commun. **11**, 4582 (2020).
[12] H. Yokota, T. Hayashida, D. Kitahara, and T. Kimura, npj Quantum Mater. **7**, 106 (2022).
[13] X. Guo, R. Owen, A. Kaczmarek, X. Fang, C. De, Y. Ahn, W. Hu, N. Agarwal, S. H. Sung, R. Hovden, S.-W. Cheong, and L. Zhao, Phys. Rev. B **107**, L180102 (2023).
[14] G. Liu, T. Qiu, K. He, Y. Liu, D. Lin, Z. Ma, Z. Huang, W. Tang, J. Xu, K. Watanabe, T. Taniguchi, L. Gao, J. Wen, J.-M. Liu, B. Yan, and X. Xi, Nat. Nanotechnol. **18**, 854 (2023).
[15] T. Higo, H. Man, D. B. Gopman, L. Wu, T. Koretsune, O. M. J. van't Erve, Y. P. Kabanov, D. Rees, Y. Li, M.-T. Suzuki, S. Patankar, M. Ikhlas, C. L. Chien, R. Arita, R. D. Shull, J. Orenstein, and S. Nakatsuji, Nat. Photon. **12**, 73 (2018).
[16] B. B. Van Aken, J.-P. Rivera, H. Schmid, and M. Fiebig, Nature (London) **449**, 702 (2007).
[17] D. Sekine, Y. Sato, and M. Matsubara, Appl. Phys. Lett. **120**, 162905 (2022).
[18] K. Kidoh, K. Tanaka, F. Marumo, and H. Takei, Acta. Crystallogr., Sect. B **40**, 329 (1984).
[19] G. Shirane, S. J. Pickart, and Y. Ishikawa, J. Phys. Soc. Jpn. **14**, 1352 (1959).
[20] H. Yamauchi, H. Hiroyoshi, M. Yamada, H. Watanabe, and H. Takei, J. Magn. Magn. Mater. **31–34**, 1071 (1983).
[21] N. A. Spaldin, M. Fechner, E. Bousquet, A. Balatsky, and L. Nordström, Phys. Rev. B **88**, 094429 (2013).
[22] S. A. Denev, T. T. A. Lummen, E. Barnes, A. Kumar, and V. Gopalan, J. Am. Ceram. Soc. **94**, 2699 (2011).
[23] M. Fiebig, V. V. Pavlov, and R. V. Pisarev, J. Opt. Soc. Am. B **22**, 96 (2005).
[24] L. Zhao, D. Torchinsky, J. Harter, A. de la Torre, and D. Hsieh, in *Encyclopedia of Modern Optics*, edited by B. D. Guenther and D. G. Steel, 2nd ed. (Elsevier, Amsterdam, 2018), Vol. 2, p. 207.
[25] M. Fiebig, D. Fröhlich, G. Sluyterman v. L., and R. V. Pisarev, Appl. Phys. Lett. **66**, 2906 (1995).
[26] M. Matsubara, A. Schmehl, J. Mannhart, D. G. Schlom, and M. Fiebig, Phys. Rev. B **81**, 214447 (2010).
[27] M. Matsubara, C. Becher, A. Schmehl, J. Mannhart, D. G. Schlom, and M. Fiebig, J. Appl. Phys. **109**, 07C309 (2011).
[28] J. G. Cherian, T. D. Tokumoto, H. Zhou, E. S. Choi, and S. A. McGill, Phys. Rev. B **87**, 214411 (2013).
[29] M. Matsubara, A. Schroer, A. Schmehl, A. Melville, C. Becher, M. Trujillo-Martinez, D. G. Schlom, J. Mannhart, J. Kroha, and M. Fiebig, Nat. Commun. **6**, 6724 (2015).
[30] L. Zhao, D. H. Torchinsky, H. Chu, V. Ivanov, R. Lifshitz, R. Flint, T. Qi, G. Cao, and D. Hsieh, Nat. Phys. **12**, 32 (2016).
[31] See Supplemental Material at http://link.aps.org/supplemental/10.1103/PhysRevMaterials.8.064406 for the calculation of SHG intensity in single- and multiferroaxial domain samples, a comparison of the polarization dependence for MD- and EQ-SHGs, and the variation of the AFM domain with respect to temperature cycling.
[32] R. R. Birss, *Symmetry and Magnetism* (North-Holland, Amsterdam, 1966).
[33] N. Bloembergen, J. Opt. Soc. Am. **70**, 1429 (1980).
[34] T. Sato, N. Abe, Y. Tokunaga, and T. Arima, Phys. Rev. B **105**, 094417 (2022).
[35] M. Fiebig, D. Fröhlich, S. Leute, and R. V. Pisarev, J. Appl. Phys. **83**, 6560 (1998).
[36] E. J. Samuelsen, M. T. Hutchings, and G. Shirane, Physica **48**, 13 (1970).
[37] Y. Todate, Y. Ishikawa, K. Tajima, S. Tomiyoshi, and H. Takei, J. Phys. Soc. Jpn. **55**, 4464 (1986).
[38] J. Akimitsu and Y. Ishikawa, J. Phys. Soc. Jpn. **42**, 462 (1977).
[39] M. Matsubara, S. Manz, M. Mochizuki, T. Kubacka, A. Iyama, N. Aliouane, T. Kimura, S. L. Johnson, D. Meier, and M. Fiebig, Science **348**, 1112 (2015).